Electronic Supplementary Material (ESI) for Journal of Materials Chemistry A.
This journal is © The Royal Society of Chemistry 2019

ESI: Pillared-layered metal-organic frameworks for mechanical energy storage applications

Jelle Wieme,[1] Sven M. J. Rogge,[1] Pascal G. Yot,[2] Louis Vanduyfhuys,[1] Su-Kyung Lee,[3] Jong-San Chang,[3] Michel Waroquier,[1] Guillaume Maurin,[2] and Veronique Van Speybroeck[1,*]

[1]*Center for Molecular Modeling, Ghent University,*
Tech Lane Ghent Science Park Campus A,
Technologiepark 46, 9052 Zwijnaarde, Belgium
[2]*Institut Charles Gerhardt Montpellier,*
Univ. Montpellier CNRS UMR 5253, CC1505,
Université de Montpellier, Place Eugène Bataillon,
F-34095 Montpellier cedex 05, France
[3]*Research Center for Nanocatalysts,*
Korea Research Institute of Chemical Technology, Yusung, Daejeon 305-600 Korea

---

[*] Veronique.VanSpeybroeck@UGent.be

Contents

I. Density-functional theory simulations

A. Computational details

DFT calculations were performed with the Vienna Ab initio Simulation Package (`VASP`) [1] using the projector-augmented wave (PAW) method [2]. The computational unit cell contains 8 metal (Zn or Cu) ions and thus 216 atoms in total. We used the PBE [3] exchange-correlation functional combined with the DFT-D3 dispersion scheme using Becke-Johnson damping [4, 5]. Recently we showed that PBE+D3(BJ)$^{\mathrm{ATM}}$ resulted in the best agreement for an energy profile as a function of volume with high-level methods for a flexible MOF. [6] Therefore, we also added three-body Axilrod-Teller-Muto (ATM) contributions [7, 8] (D3(BJ)$^{\mathrm{ATM}}$) a posteriori to the energy with the DFT-D3 program [9] as they have not yet been implemented in `VASP`. This is justified by the typically small corrections to the geometry [6, 10]. We employed the recommended GW PBE PAW potentials for all elements and functionals (v5.4). For the Zn and Cu atoms, 3s, 3p, 3d and 4s electrons were explicitly included. For the C and O atoms the 2s and 2p electrons were considered as valence electrons. For the H atoms, the 1s electron was treated as a valence electron. All DFT calculations were performed with a plane-wave kinetic-energy cutoff of 600 eV and using Gaussian smearing with a smearing width of 0.05 eV. Projection operators were evaluated in reciprocal space. A 2×2×2 Monkhorst-Pack k-grid was used for the volumes in the open-pore and large-pore states. A denser grid was used for lower volumes (2×2×5). The real-space FFT grid was able to describe wavevectors up to two times the maximum wavevector present in the basis set. An augmentation grid that is twice as large was used to avoid wrap-around errors in order to obtain accurate forces. The electronic (ionic) convergence criterion was set to 10^{-8} (10^{-7}) eV. The energy profile as a function of volume was constructed by fixed-volume relaxations in which the positions and cell shape were optimized [11]. We also calculated the dynamical matrix using 0.01 Å displacements for all atomic coordinates for the stable open-pore phase of DMOF-1(Zn).

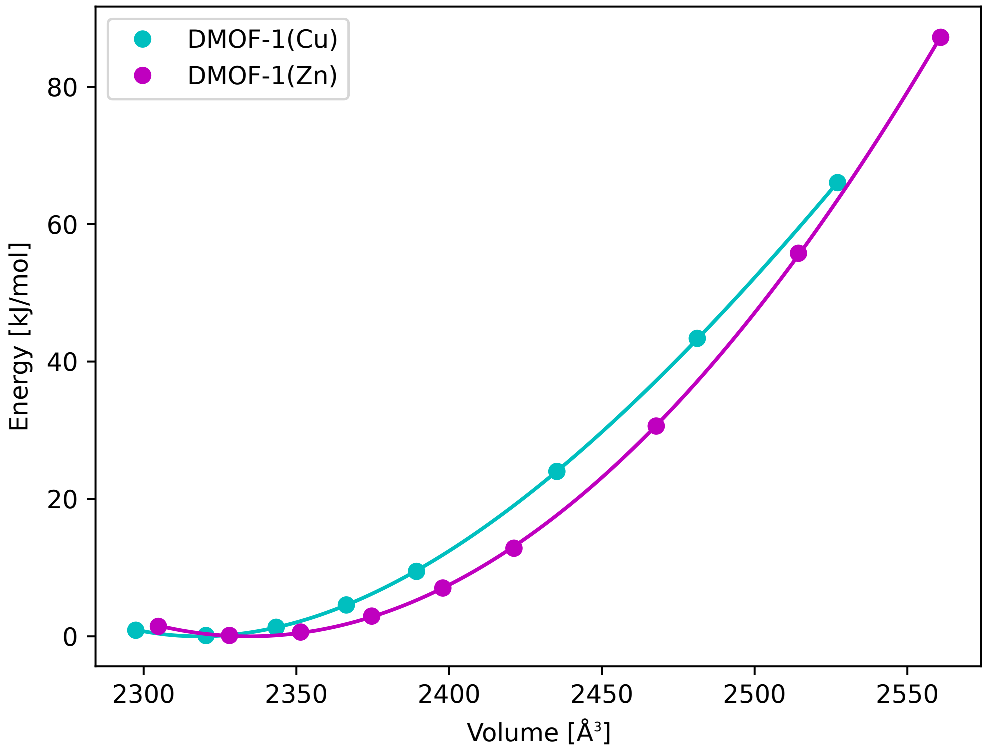

FIG. 1. A local energy profile (PBE+D3(BJ)$^{\mathrm{ATM}}$) as a function of the volume for DMOF-1(Zn) and DMOF-1(Cu) fitted to a Rose-Vinet equation of state. [11, 12]

B. Local energy profile as a function of the volume

We constructed for DMOF-1(Zn) and DMOF-1(Cu) (in its preferred magnetic configuration, see further) a local energy profile as a function of volume [11] to obtain the equilibrium volume and bulk modulus. We did this by fitting the DFT data to the Rose-Vinet equation of state. [12] As the structure changes from a tetragonal to an orthorhombic lattice system, we only included data points in our fit belonging to the tetragonal structure at the equilibrium volume. The data points and fit are shown in Fig. 3. The resulting fit parameters are tabulated in Table 1 (main article).

TABLE I. The resulting coupling constants for the magnetic interactions in DMOF-1(Cu) along the dabco linker J_{dabco}, the bdc linker J_{bdc} and in the paddle wheel J_{pw}. They were obtained by fitting them with a least-squares approach.

J_{bdc} [meV]	J_{dabco} [meV]	J_{pw} [meV]
0.5	0.5	-133.6

C. Magnetic configurations of DMOF-1(Cu)

Following a similar approach as Vanpoucke *et al.*, [13] we describe magnetism by the coupling of local spins at distinguishable magnetic centers through the Heisenberg-Dirac-Van Vleck Hamiltonian $\hat{H}$ [14–16]:

$$\hat{H} = -\sum_{i,j} J_{ij} S_i \cdot S_j. \tag{1}$$

The neighboring spins are coupled with a coupling constant J_{ij}. $\vec{S}_i$ is the spin operator applied on magnetic center i and projected along the z-direction. In other words, we map the DFT energies on a 1D Ising model. We take three coupling interactions into account: the coupling along the dabco linker between two copper metal centers J_{dabco}, the coupling along the bdc linker between two copper metal centers J_{bdc} and the coupling between two copper centers in the paddle wheel J_{pw}. Our computational unit cell contains four copper paddle wheels, and thus eight copper centers with one unpaired electron. We use a spin 1/2 based on the presence of this one unpaired electron.

We consider different spin configurations (see Fig. 2) that have different eigenvalues E for the Hamiltonian, and use a least-squares approach to fit the unknown coupling constants in this overdetermined system of six equations (one for each spin configuration). A negative value indicates a ferromagnetic coupling, while a negative value signifies an antiferromagnetic coupling. Table I presents the results. We thus find that along the organic bdc and dabco ligands there is a negligible ferromagnetic coupling, while in the groundstate the copper ions in the paddle wheel interact antiferromagnetically. These findings are in agreement with experimental measurements. [17]

The above discussion was performed on the basis of comparing energies between optimized

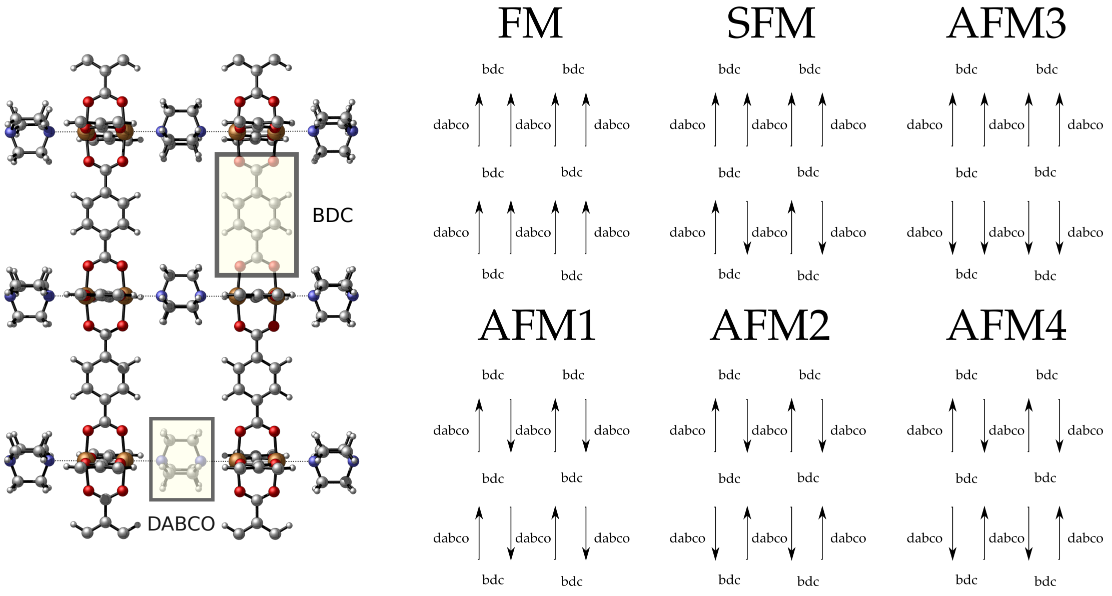

FIG. 2. The six spin configurations that were used to model the magnetism in DMOF-1(Cu) together with the atomistic structure of DMOF-1(Cu).

structures at fixed volumes. We also constructed a local energy profile as a function of the volume for all different magnetic configurations. As shown in Fig. 3, the minimum and the curvature are not really affected by the type of magnetic interactions. Therefore, we don't observe a lot of spread in the equation-of-state parameters for the different magnetic configurations. The magnetic interactions are local, i.e., limited to the paddle wheel, and this is reflected as a constant shift of the energy profiles without a strong volume dependence.

D. Closed pore state of DMOF-1(Cu)

Fig. 4 displays a molecular representation of the one-dimensional channel of the cp state of DMOF-1(Cu) obtained at the PBE+D3(BJ) level of theory.

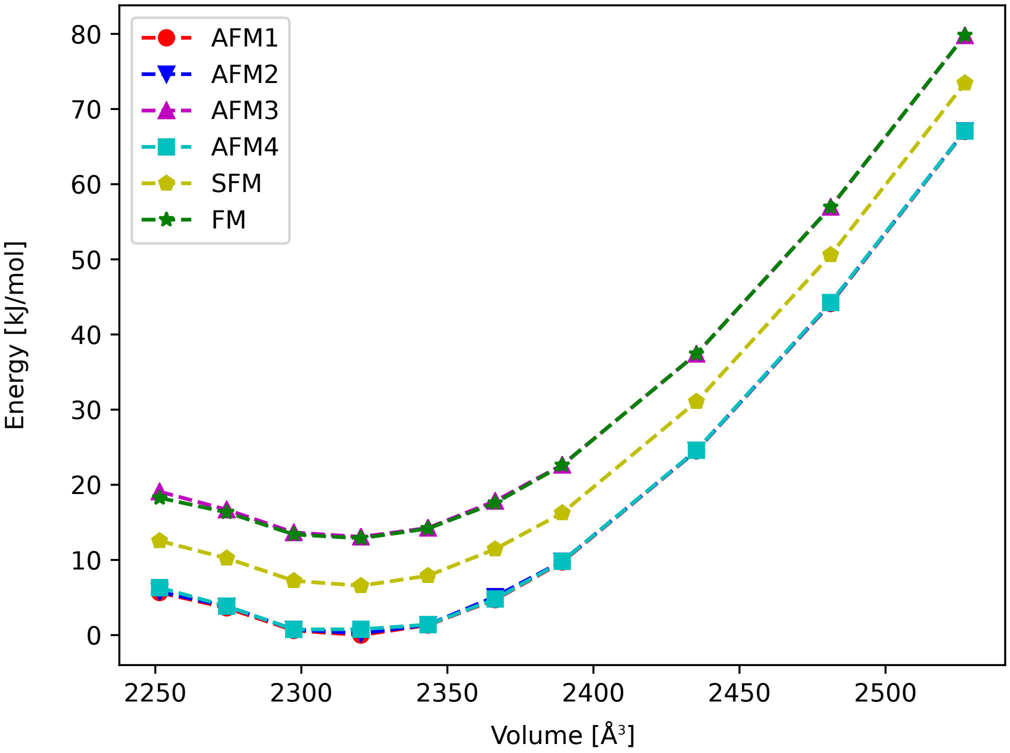

FIG. 3. A local energy profile as a function of the volume for the different magnetic configurations of DMOF-1(Cu). The definition of the magnetic configurations is given in Fig. 2.

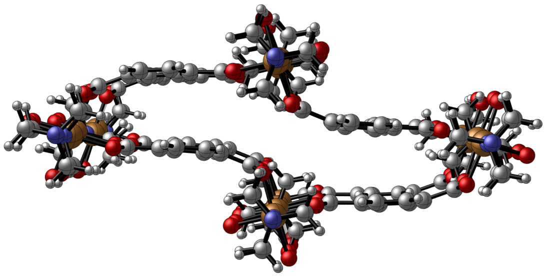

FIG. 4. Molecular representation of the cp state of DMOF-1(Cu) obtained at the PBE+D3(BJ) level of theory.

II. Force field simulations

A. Force field derivation

The first-principles force fields used to model our systems are derived using `QuickFF` [18, 19], a software package developed by some of the present authors. Within this protocol, the quantum mechanical potential energy surface (PES) is approximated by a sum of analytical functions of the nuclear coordinates that describe the covalent (cov) and noncovalent (noncov) interactions. The latter is composed of electrostatic and van der Waals interactions.

$$V^{FF} = \underbrace{V_{bond} + V_{bend} + V_{oopd} + V_{torsion} + V_{cross}}_{V_{cov}} + V_{ei} + V_{vdW}. \tag{2}$$

1. *First-principles periodic data*

Just as in our previous work on MOFs[19, 20], we use periodic models to generate the required first-principles input data. As described above, we used the dynamical matrix calculated on the open-pore phase of DMOF-1(Zn).

2. *Covalent interactions*

The covalent interactions – which mimic the chemical bonds between the atoms – are approximated by different terms as a function of the internal coordinates (bonds, bends, out-of-plane distances, and dihedrals). The unknown force field parameters are fitted following the most recent `QuickFF` procedure. [18, 19] The harmonic bond and bend terms are given by:

$$V_{\text{bond}}^{ij} = \frac{K_{ij}}{2} \left(r_{ij} - r_{0,ij}\right)^2, \tag{3}$$

$$V_{\text{bend}}^{ijk} = \frac{K_{ijk}}{2} \left(\theta_{ijk} - \theta_{0,ijk}\right)^2. \tag{4}$$

For methane, only harmonic bonds and bends were used. We also add cross terms between the bonds and bends to improve the correspondence with the first-principles data. [19] The included cross terms are:

- angle stretch-stretch terms (ASS) between neigboring bonds, *i.e.* part of the same angle

- angle stretch-angle terms (ASA).

The mathematical expression of these terms is given by

$$V_{\mathrm{ASS}}^{ijk} = K_{ijk}^{\mathrm{ASS}} \left(r_{ij} - r_{0,ij}\right)\left(r_{jk} - r_{0,jk}\right) \tag{5}$$

$$V_{\mathrm{ASA}}^{ijk} = \left[K_{ijk}^{\mathrm{ASA1}} \left(r_{ij} - r_{0,ij}\right) + K_{ijk}^{\mathrm{ASA2}} \left(r_{jk} - r_{0,jk}\right)\right]\left(\theta_{ijk} - \theta_{0,ijk}\right). \tag{6}$$

The out-of-plane distances are described using a harmonic potential:

$$V_{oopd}^{ijkl} = \frac{K_{ijkl}}{2}\left(d_{ijkl} - d_{0,ijkl}\right)^2. \tag{7}$$

This is a four-atom interaction, in which the internal coordinate is the distance between the central atom and the plane determined by its three neighbors. The fourth covalent term is the dihedral energy term. Here, a cosine term is used as a function of the dihedral angle, including the multiplicity m_ϕ of the dihedral angle:

$$V_{torsion}^{ijkl} = \frac{K_{ijkl}}{2}\left[1 - \cos(m_\phi(\phi_{ijkl} - \phi_{0,ijkl}))\right]. \tag{8}$$

The unknown parameters in all terms (force constants, rest values, and multiplicities) in the covalent energy expression can be estimated directly with `QuickFF`.

3. Electrostatic interactions

The electrostatic interactions are modeled by a Coulomb interaction between Gaussian charge distributions, [21] which allow to include all pairwise interactions. The atomic charges q_i are derived with the Minimal Basis Iterative Stockholder (MBIS) partitioning scheme [22].

$$V_{ei} = \frac{1}{2}\sum_{\substack{i,j=1\\(i\neq j)}} \frac{q_i q_j}{4\pi\epsilon_0 r_{ij}} \operatorname{erf}\left(\frac{r_{ij}}{d_{ij}}\right) \tag{9}$$

Gaussian charge distributions are used with a total charge q_i and radius d_i, centered on atom i. The mixed radius of the Gaussian charges, [21] d_{ij}, is given by $\sqrt{d_i^2 + d_j^2}$. The interaction depends on the distance r_{ij} between the two atoms.

4. Van der Waals interactions

The van der Waals interactions are described by the MM3-Buckingham model [23, 24] up to a finite cutoff (12 Å) and are supplemented with tail corrections. [25]

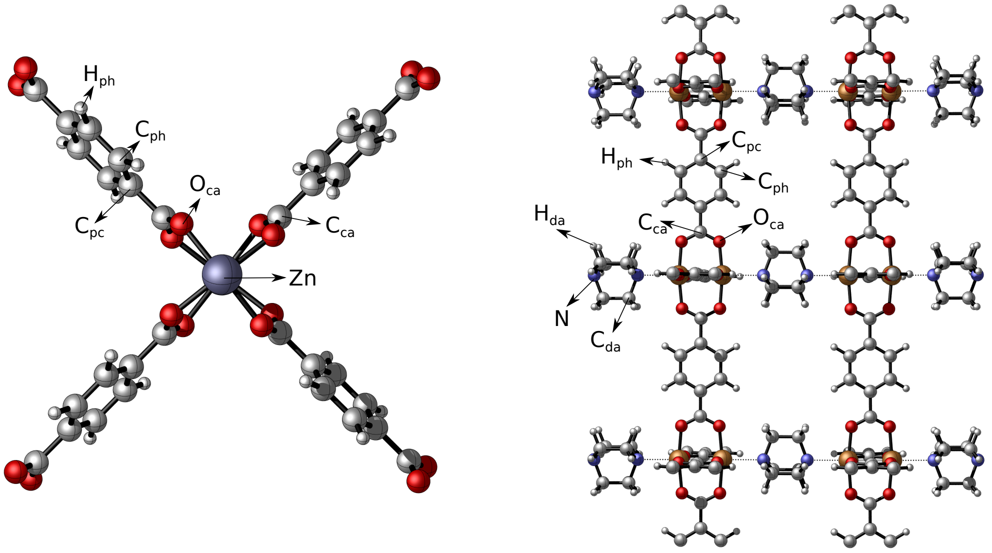

FIG. 5. Definition of the atom types used in the DMOF-1(Zn) force field.

$$V_{vdW} = \epsilon_{ij} \left[1.84 \cdot 10^5 \exp\left(-12 \frac{r}{\sigma_{ij}} \right) - 2.25 \left(\frac{\sigma_{ij}}{r} \right)^6 \right] \tag{10}$$

The two parameters σ_{ij} and ϵ_{ij} are the equilibrium distance and the well depth of the potential. These parameters are typically determined with empirical mixing rules for the interaction between atom i and atom j:

$$\sigma_{ij} = \sigma_i + \sigma_j \qquad \text{and} \qquad \epsilon_{ij} = \sqrt{\epsilon_i \epsilon_j} \tag{11}$$

and these parameters were taken from the MM3 force field for every atom and are tabulated in Ref. 24. In MM3, the 1-2 and 1-3 interactions are discarded to avoid a strong overestimation of the repulsion terms.

5. *Force field parameters*

The force field parameters are listed in Tables II, III, IV and V. Figure 5 displays the definition of the atom types used in the DMOF-1(Zn) force field.

TABLE II. Parameters of the covalent bond and bend contributions to the DMOF-1(Zn) force field.

bonds	K_{ij} [kJ/(mol·Å^2)]	$r_{0,ij}$ [Å]
$\mathrm{O_{ca} - Zn}$	568	2.076
$\mathrm{C_{ca} - O_{ca}}$	5301	1.278
$\mathrm{C_{ca} - C_{pc}}$	2545	1.498
$\mathrm{C_{ph} - H_{ph}}$	3216	1.092
$\mathrm{C_{pc} - C_{ph}}$	3793	1.396
$\mathrm{C_{da} - H_{da}}$	3023	1.097
$\mathrm{C_{da} - C_{da}}$	2290	1.543
$\mathrm{C_{ph} - C_{ph}}$	4020	1.391
$\mathrm{N - Zn}$	750	2.055
$\mathrm{C_{da} - N}$	2519	1.479
bends	K_{ijk} [kJ/(mol·rad^2)]	$\theta_{0,ijk}$ [deg]
$\mathrm{C_{da} - N - C_{da}}$	764	108.7
$\mathrm{O_{ca} - C_{ca} - O_{ca}}$	683	124.8
$\mathrm{N - Zn - O_{ca}}$	88	105.5
$\mathrm{H_{da} - C_{da} - N}$	430	106.7
$\mathrm{H_{da} - C_{da} - H_{da}}$	296	108.0
$\mathrm{C_{ph} - C_{ph} - H_{ph}}$	247	121.8
$\mathrm{C_{da} - C_{da} - H_{da}}$	300	111.7
$\mathrm{C_{pc} - C_{ca} - O_{ca}}$	623	117.7
$\mathrm{C_{ca} - O_{ca} - Zn}$	102	122.2
$\mathrm{C_{ca} - C_{pc} - C_{ph}}$	379	119.4
$\mathrm{C_{da} - N - Zn}$	72	102.7
$\mathrm{C_{ph} - C_{pc} - C_{ph}}$	509	120.0
$\mathrm{C_{pc} - C_{ph} - H_{ph}}$	262	117.1
$\mathrm{C_{pc} - C_{ph} - C_{ph}}$	556	120.2
$\mathrm{C_{da} - C_{da} - N}$	680	109.8

TABLE III. Parameters of the covalent dihedral and out-of-plane-distance contributions to the DMOF-1(Zn) force field.

dihedrals	K_{ijkl} [kJ/mol]	$\phi_{0,ijkl}$ [deg]	m_ϕ
$C_{ph} - C_{pc} - C_{ph} - C_{ph}$	29.5	0	2
$C_{pc} - C_{ph} - C_{ph} - H_{ph}$	32.7	0	2
$C_{ca} - C_{pc} - C_{ph} - C_{ph}$	43.4	0	2
$C_{ph} - C_{pc} - C_{ph} - H_{ph}$	26.7	0	2
$H_{ph} - C_{ph} - C_{ph} - H_{ph}$	18.1	0	2
$C_{pc} - C_{ca} - O_{ca} - Zn$	15.8	0	2
$O_{ca} - C_{ca} - O_{ca} - Zn$	9.0	0	2
$C_{pc} - C_{ph} - C_{ph} - C_{pc}$	35.1	0	2
$C_{ph} - C_{pc} - C_{ca} - O_{ca}$	11.2	0	2
$C_{ca} - C_{pc} - C_{ph} - H_{ph}$	22.0	0	2
$N - C_{da} - C_{da} - N$	10.7	0	3
$C_{da} - N - C_{da} - H_{da}$	1.5	60	3
$C_{da} - C_{da} - N - C_{da}$	3.2	60	3
$H_{da} - C_{da} - N - Zn$	4.7	60	3
$C_{da} - C_{da} - N - Zn$	39.4	60	3
out-of-plane-distances	K_{ijkl} [kJ/(mol·Å^2)]	$d_{0,ijkl}$ [Å]	
$C_{ca} - C_{ph} - C_{ph} - C_{pc}$	101	0.0	
$C_{pc} - O_{ca} - O_{ca} - C_{ca}$	1278	0.0	
$C_{pc} - C_{ph} - H_{ph} - C_{ph}$	111	0.0	

TABLE IV. Parameters of the covalent cross term contributions to the DMOF-1(Zn) force field.

dihedrals	K_{ijk}^{ASS} [kJ/(mol·Å^2)]	K_{ijk}^{ASA1} [kJ/(mol·rad)]	K_{ijk}^{ASA2} [kJ/(mol·rad)]	$r_{0,ij}$ [Å]	$r_{0,jk}$ [Å]	$\theta_{0,ijk}$ [deg]
$\mathrm{C_{ca} - O_{ca} - Zn}$	217	18	22	1.278	2.057	123.8
$\mathrm{O_{ca} - Zn - O_{ca}}$	82	41	41	2.057	2.057	113.4
$\mathrm{O_{ca} - Zn - Zn}$	-27	-47	-21	2.057	2.960	81.6
$\mathrm{N - Zn - Zn}$	-20	0	0	2.067	2.067	180.0
$\mathrm{O_{ca} - C_{ca} - O_{ca}}$	761	410	410	1.278	1.278	125
$\mathrm{C_{pc} - C_{ca} - O_{ca}}$	374	172	434	1.496	1.278	117.8
$\mathrm{C_{ca} - C_{pc} - C_{ph}}$	311	139	78	1.496	1.398	120.1
$\mathrm{C_{ph} - C_{pc} - C_{ph}}$	549	21	21	1.398	1.398	119.3
$\mathrm{C_{pc} - C_{ph} - H_{ph}}$	55	71	149	1.398	1.091	117.4
$\mathrm{C_{ph} - C_{ph} - H_{ph}}$	47	83	113	1.391	1.091	121.7
$\mathrm{C_{pc} - C_{ph} - C_{ph}}$	511	52	85	1.398	1.391	120.4
$\mathrm{H_{da} - C_{da} - H_{da}}$	22	84	84	1.097	1.097	108.5
$\mathrm{C_{da} - C_{da} - H_{da}}$	28	123	77	1.546	1.097	112.1
$\mathrm{H_{da} - C_{da} - N}$	61	76	174	1.097	1.483	106.7
$\mathrm{C_{da} - C_{da} - N}$	179	181	277	1.546	1.483	110.0
$\mathrm{C_{da} - N - Zn}$	156	23	50	1.483	2.067	110.0
$\mathrm{C_{da} - N - C_{da}}$	183	239	239	1.483	1.483	108.6

TABLE V. Parameters of the noncovalent contributions to DMOF-1(Zn) force field.

Atom type	q_i [e]	d_i [Å]	ϵ [kcal/mol]	σ [Å]
Zn	0.985	2.073	0.276	2.290
$\mathrm{H_{ph}}$	0.135	0.731	0.020	1.620
$\mathrm{C_{ca}}$	0.749	1.165	0.056	1.940
N	-0.308	1.104	0.043	1.930
$\mathrm{C_{pc}}$	-0.117	1.165	0.056	1.940
$\mathrm{H_{da}}$	0.134	0.731	0.020	1.620
$\mathrm{C_{da}}$	-0.104	1.165	0.027	2.040
$\mathrm{O_{ca}}$	-0.631	1.133	0.059	1.820
$\mathrm{C_{ph}}$	-0.113	1.165	0.056	1.960

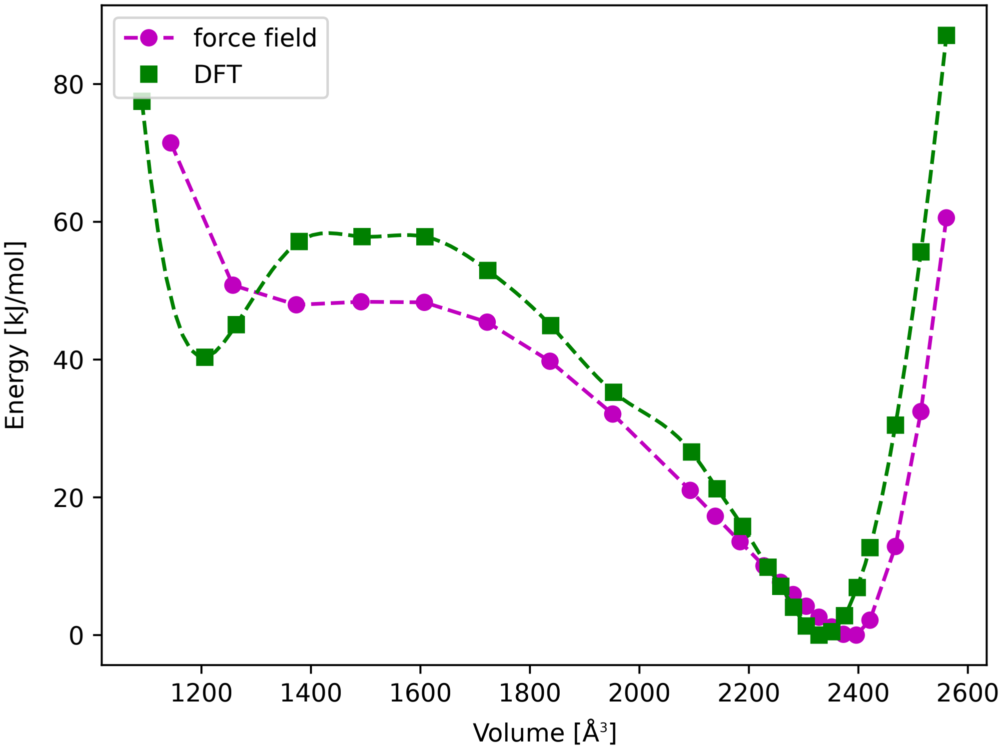

FIG. 6. A comparison between the DFT and force field energy profile as a function of the volume at 0 K of DMOF-1(Zn).

B. Validation

Previously, similar `QuickFF` force fields have been successfully applied to a wide range of MOFs for various properties such as lattice parameters, bulk moduli, elastic constants, and free energy profiles. [20, 26, 27] To validate the force field in this work, we compared the first-principles results with those obtained by the new force field. In this subsection, we investigate if the force field is able to at least qualitatively reproduce the 0 K DFT results. Therefore, we constructed an energy profile $E(V)$ as a function of the volume at 0 K to directly compare with our DFT profile. To this end, we start by optimizing the DFT structures with our new force field using the fixed volume optimizer as implemented in `ASE`. [28] The results are shown in Fig. 6.

It is clear that the force field displays a good agreement around the DFT minimum in the

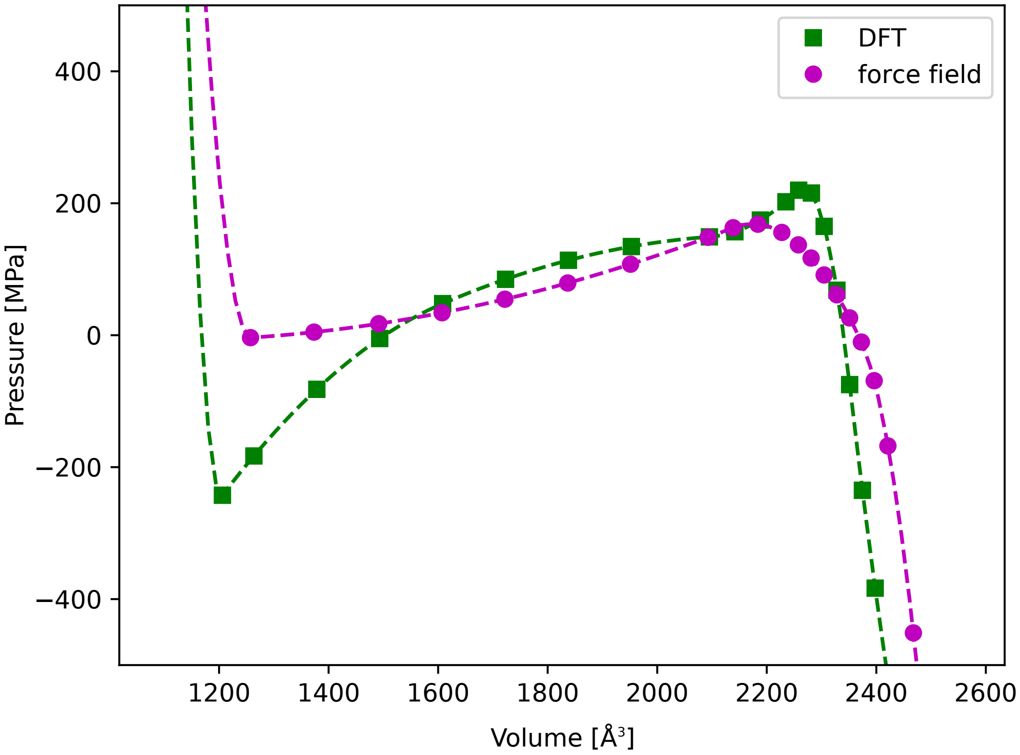

FIG. 7. A comparison between the DFT and force field pressure profile as a function of the volume at 0 K of DMOF-1(Zn).

open-pore state (to which it was fitted). At volumes below 1800 Å^3, the difference becomes larger. At even lower volumes, i.e., in the closed-pore phase, the DFT simulations predict a very stable minimum in contrast to the force field. The force field is not able to precisely reproduce this dense structure, as it is subject to strong local deformations in the N-Zn–Zn-N coordination environment [29], which are not captured in the force field fitting procedure. Moreover, no many-body dispersion interactions are included in the force field in contrast to the DFT simulations. Nevertheless, it is clear that the force field also predicts a contraction towards a dense state above a transition pressure. Therefore, Fig. 7 shows that the pressure profile $P(V)$ as function of the volume displays the same qualitative behavior. Hence, this force field was used to assess the influence of temperature on the pressure-induced breathing transition. Furthermore, Figs. 8 and 9 illustrate that the force field optimized structures resemble the DFT structures.

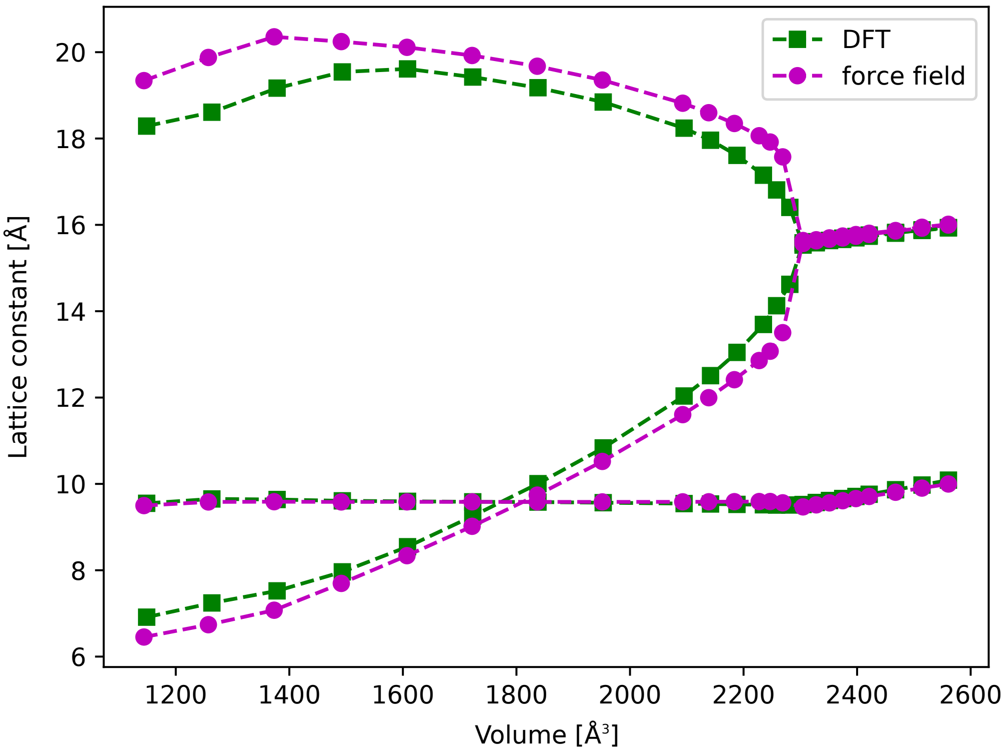

FIG. 8. A comparison between the static DFT optimized and force field lattice constants for different volumes of DMOF-1(Zn).

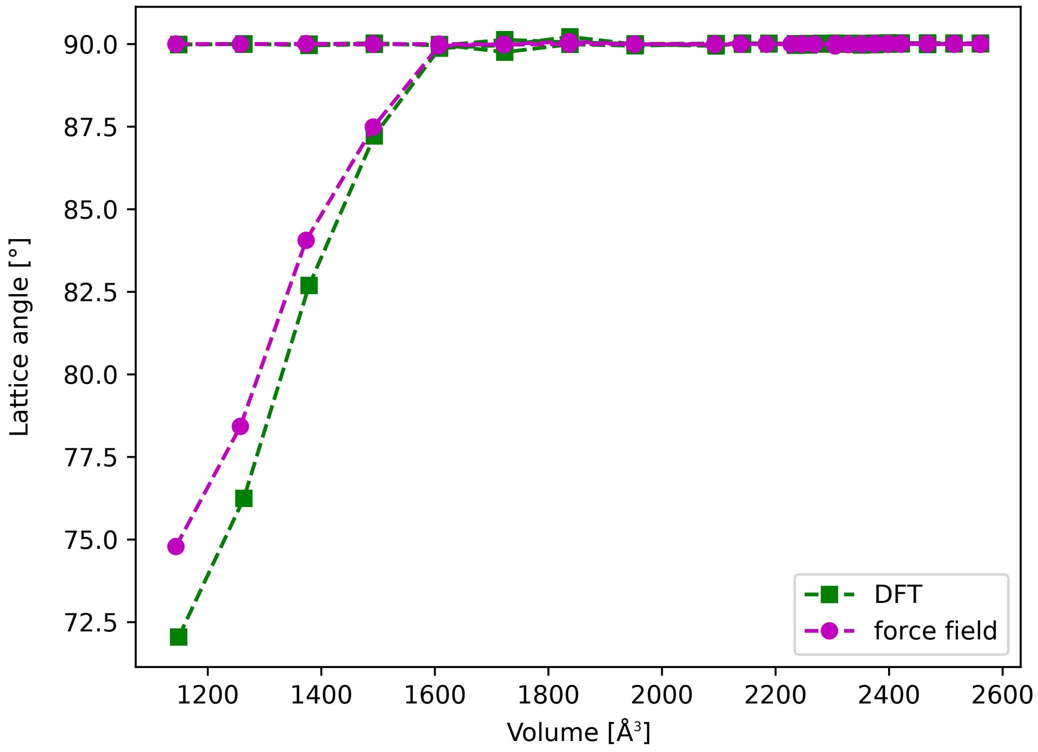

FIG. 9. A comparison between the static DFT optimized and force field lattice angles for different volumes of DMOF-1(Zn).

C. Molecular dynamics (MD) simulations

The DMOF-1(Zn) force field was used to perform MD simulations in the $(N, V, \boldsymbol{\sigma}_\mathbf{a}{=}\mathbf{0}, T)$ and $(N, P, \boldsymbol{\sigma}_\mathbf{a}{=}\mathbf{0}, T)$ ensembles. [30] Simulations were carried out for different volumes at a temperature of 150 K, 300 K and 450 K. We constructed the pressure profile $P(V)$ and Helmholtz free energy profile $F(V)$ as a function of the volume for these temperatures, and these results are taken up in the main manuscript. More details on the simulation protocol to construct these profiles can be found elsewhere. [20, 30] In this section, we illustrate the effect of temperature on the XRD patterns and hint towards reduced symmetry using radial distribution functions.

1. X-ray diffraction patterns

X-ray diffraction (XRD) patterns were calculated with CSD Python API [31]. For the DFT simulations, we calculated the pattern for the optimized structure at different volumes (for the different phases, see Fig. 2 in the main manuscript). For the force field MD simulations, we took 100 snapshots from $(N, V, \boldsymbol{\sigma}_\mathbf{a}{=}\mathbf{0}, T)$ simulations at different volumes at 300 K and averaged the calculated XRD patterns. In an experimental setup, the XRD patterns would slightly change as a function of temperature due to thermal expansion behavior. Here, we only illustrate the effect of the mobility of the atoms at 300 K as compared to a static optimized structure at 0 K.

In Figure 10, we compare the XRD patterns obtained with both techniques. It is immediately obvious that the mobility of the atoms (at a specific volume) has only a minor impact on the XRD pattern. The XRD patterns differ at low volumes in the cp phase, but as shown above, this is the region in which the force field performs not so well. Therefore, to predict how the XRD patterns will evolve as a function of pressure/volume in an experiment for DMOF-1, one could limit themselves to optimizing different structures at 0 K.

2. Radial distribution functions

We determined the radial distribution functions (RDFs) [27] of the different atoms in DMOF-1(Zn) with respect to the center of the zinc paddlewheel cluster at 300 K for three

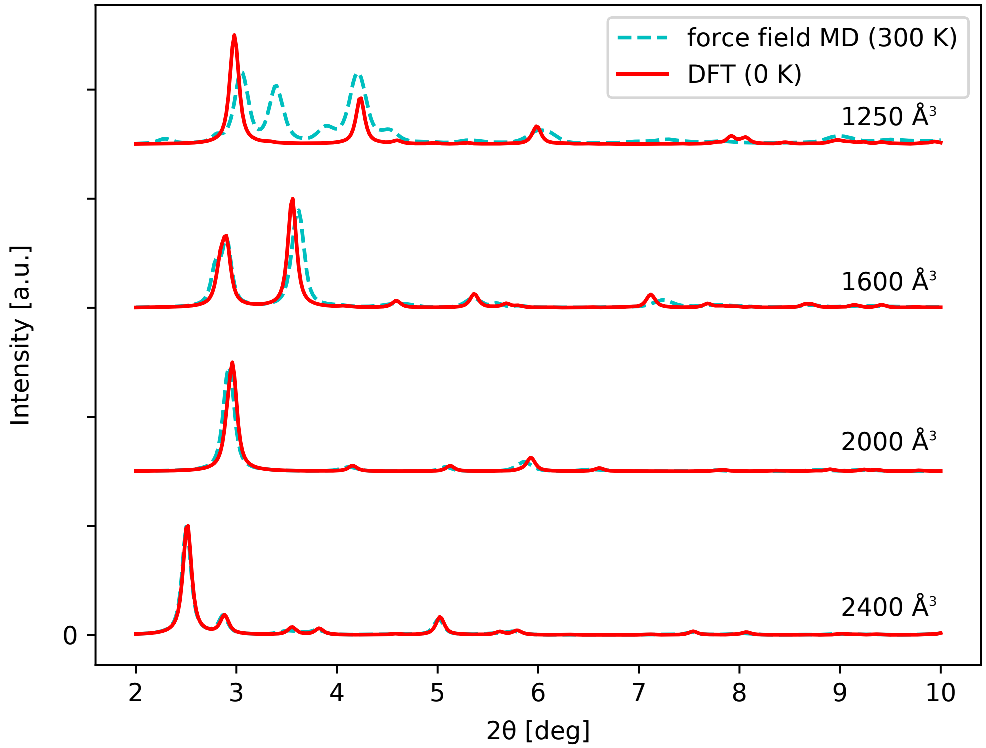

FIG. 10. A comparison between the static DFT optimized and force field MD X-ray diffraction pattern for different volumes of DMOF-1(Zn) (λ=0.4859 Å).

volumes: at 2400 Å^3 (tetragonal), at 1800 Å^3 (orthorhombic), and at 1270 Å^3 (monoclinic) (Fig. 11). The RDFs in the tetragonal and orthorhombic phases are defined by well-defined peaks for distances up to about 10 Å. At a volume of 1800 Å^3, the new zinc peak at 10 Å is a direct result of the decreased symmetry when going from the tetragonal to the orthorhombic phase. When going to the contracted monoclinic phase at 1270 Å^3, the peaks are much more spread out and start to overlap, revealing that the symmetry of this contracted phase is reduced.

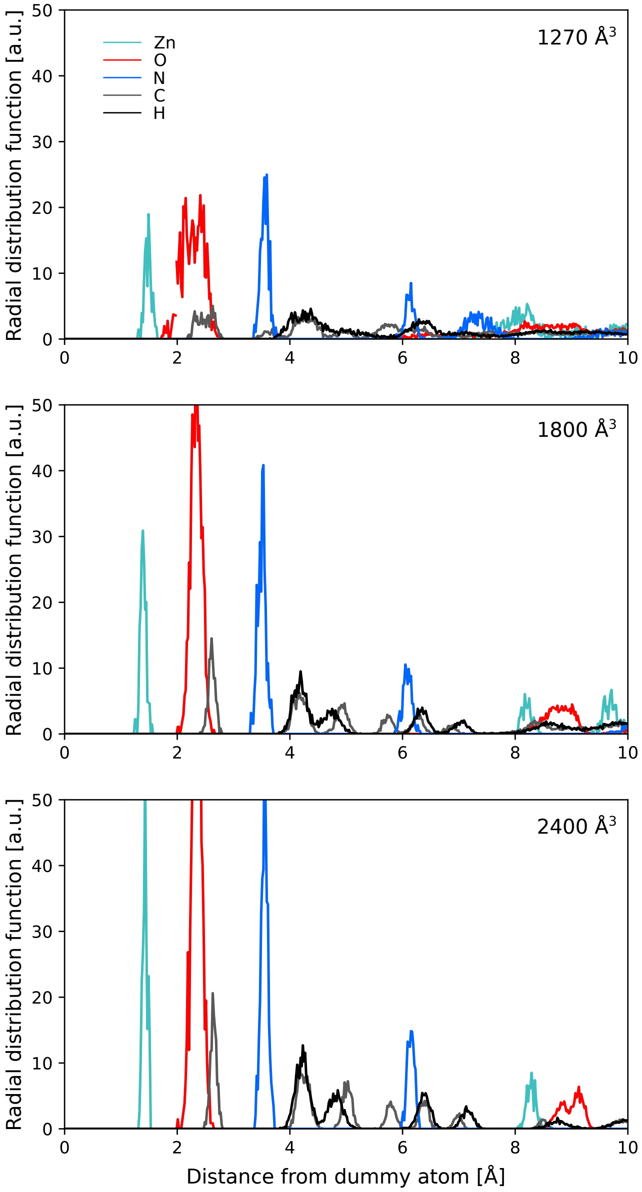

FIG. 11. Radial distribution functions of the different atoms in DMOF-1(Zn) with respect to the center of the zinc paddlewheel cluster at 300 K for three volumes: at 2400 Å^3 (tetragonal), at 1800 Å^3 (orthorhombic), and at 1270 Å^3 (monoclinic).

III. Experiment

After synthesis and activation as described in the main article, the powder X-ray diffraction pattern of DMOF-1(Zn/Cu) was obtained by Rigaku diffractometer (D/MAX IIIB, 2 kW) using Ni-filtered Cu-K$_{\alpha 1}$-radiation (40 kV, 30 mA, λ=1.54059 Å) and a graphite crystal monochromator. The particle morphology and crystal size were analyzed by a scanning electron microscope (SEM, Philips, XL30S FEG). The assessment of the accessible surface was performed with N_2 adsorption-desorption isotherms at -196°C after dehydration under vacuum at -150°C for 12 hours using a Micromeritics Tristar 3020. The specific surface areas were evaluated using the Brunauer-Emmett-Teller (BET) method and the pore volume was taken by a single point method at p/p_0=0.99. The BET area and pore volume were found to be very similar for both DMOF-1(Zn) (1660 m^2/g and 0.74 cm^3/g) and DMOF-1(Cu) (1460 m^2/g and 0.74 cm^3/g) samples, consistent with previous findings.[32–34]

The DMOF-1(Cu) and DMOF-1(Zn) samples were evacuated under secondary vacuum during 8 hours at 150°C. The sample preparations were performed using a glove box (Jacomex P-BOX) under argon atmosphere (H_2O < 1 ppm) to avoid the rehydration of the solid. The structural features of DMOF-1(Cu) and DMOF-1(Zn) were investigated by laboratory X-ray diffraction (XRD) using a PANalytical X'Pert equipped with an X'Celerator detector and a Si (111) monochromator (Cu-K$_{\alpha 1}$ wavelength, λ=1.54059 Å with an operating voltage of 40 kV and a beam current of 40 mA). The samples were evacuated into a 1 mm glass capillary in the glove box and sealed before collecting its X-ray powder diffraction (PXRD) pattern (Fig. 12 and Fig. 13). These diffraction patterns were successfully indexed in the tetragonal system with the space group $P4/nbm$ (No. 125). The resulting unit cell parameters and associated volumes were obtained using a LeBail fit by the Jana2006 software (Table VI). [35]

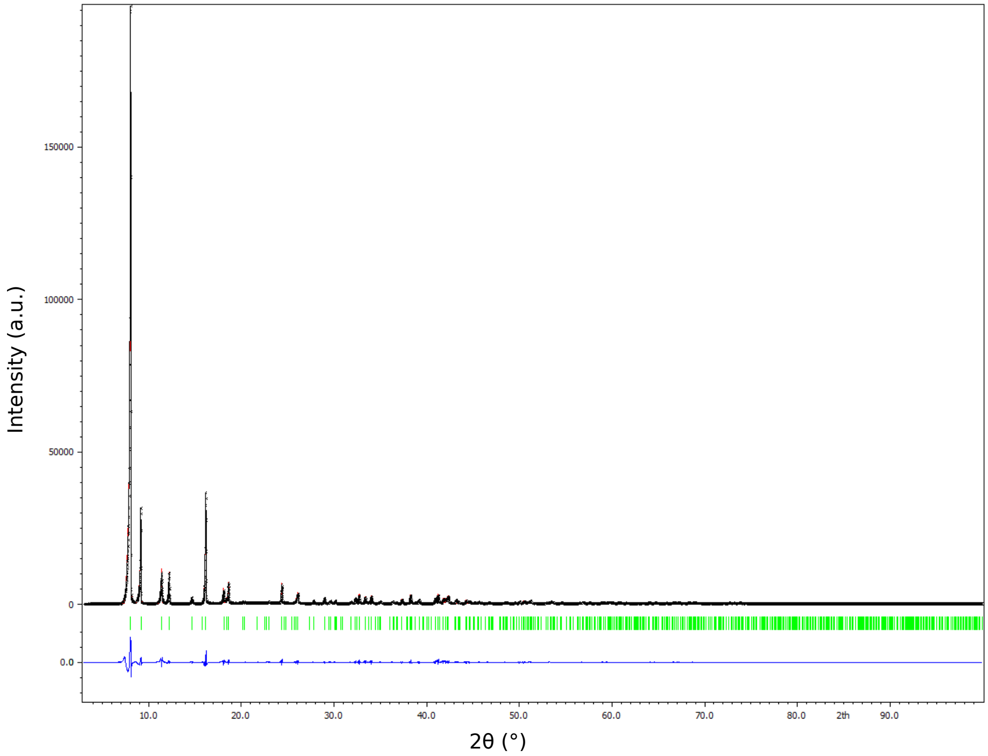

FIG. 12. Laboratory X-ray diffraction pattern (λ=1.54059 Å) indexed in the tetragonal system with the space group *P*4/*nbm* (No. 125). The resulting unit cell parameters ($a = b$ =15.4610(3) Å and c=9.6215(2) Å) and associated volume (2301.1(1) Å^3) were obtained using a LeBail fit (GoF=4.2. Rp=10.18, wRp=14.82).

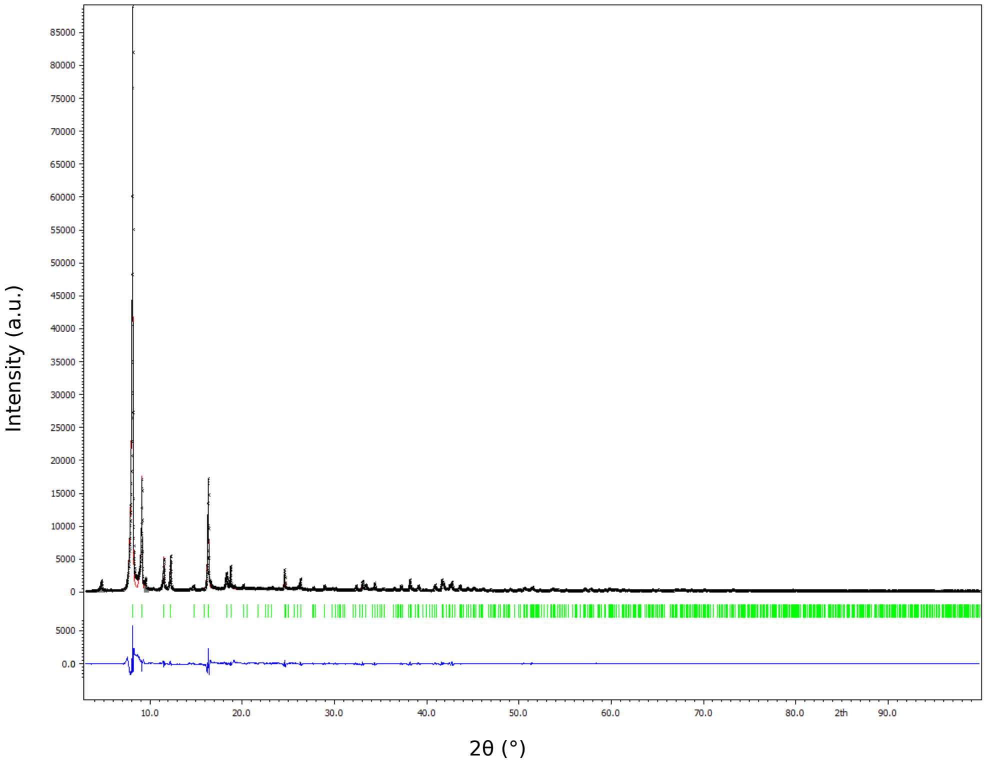

FIG. 13. Laboratory X-ray diffraction pattern (λ=1.54059 Å) indexed in the tetragonal system with the space group $P4/nbm$ (No. 125). The resulting unit cell parameters ($a = b$ =15.3208(6) Å and c=9.6522(4) Å) and associated volume (2266.2(1) Å^3) were obtained using a LeBail fit (GoF=3.66, Rp=10.43, wRp=15.53).

The compression of the two solids was carried out using a Hg-porosimeter Micromeritics Autopore 9500 ($P \leq 420$ MPa) where non-wetting mercury (which cannot penetrate into the pores) acts as an hydrostatic tranmitting media on the crystallites. Two sets of experiments were performed for both materials in order to reveal the possible impact of the kinetics: (i) two consecutive compression-decompression cycles and (ii) two compression-decompression cycles separated by 48 hours. Irreversible pressure-induced structural contraction was observed for both scenarios at the same pressure and associated volume change that clearly discard the influence of the kinetics on the structural behavior of the two phases under the application of mechanical pressure and its release. All the corresponding data are summarized in Table VI and Figure 14.

TABLE VI. Unit cell parameters determined for the pristine DMOF-1(Zn/Cu) from the PXRD pattern. Transition pressures and associated volume changes, as well as bulk moduli derived from the mercury intrusion experiments (compression curves).

Solids	DMOF-1(Zn)		DMOF-1(Cu)	
Space group	$P4/nbm$ (No. 125)			
a (Å)	15.4610(3)		15.3208(6)	
c (Å)	9.6215(2)		9.6522(4)	
V (Å^3)	2301.1(1)		2266.2(1)	
B_0 (GPa)	16.9		18.8	
	2 consecutive cycles	2 separated cycles	2 consecutive cycles	2 separated cycles
P_{max} (MPa)	51	51	193	193
V (Å^3) (contracted)	1194.9	1281.9	1504.6	1487.7
ΔV (%)	48.1	44.3	33.6	34.4
Energy work (J/g)	29.9	27.5	78.1	79.9
Number of formula per unit cell Z	2			
Molar mass M (g/mol)	567.52		569.36	
Slope of the mercury intrusion curve α (mL/(g·MPa))	7.19×10^{-5}		6.37×10^{-5}	

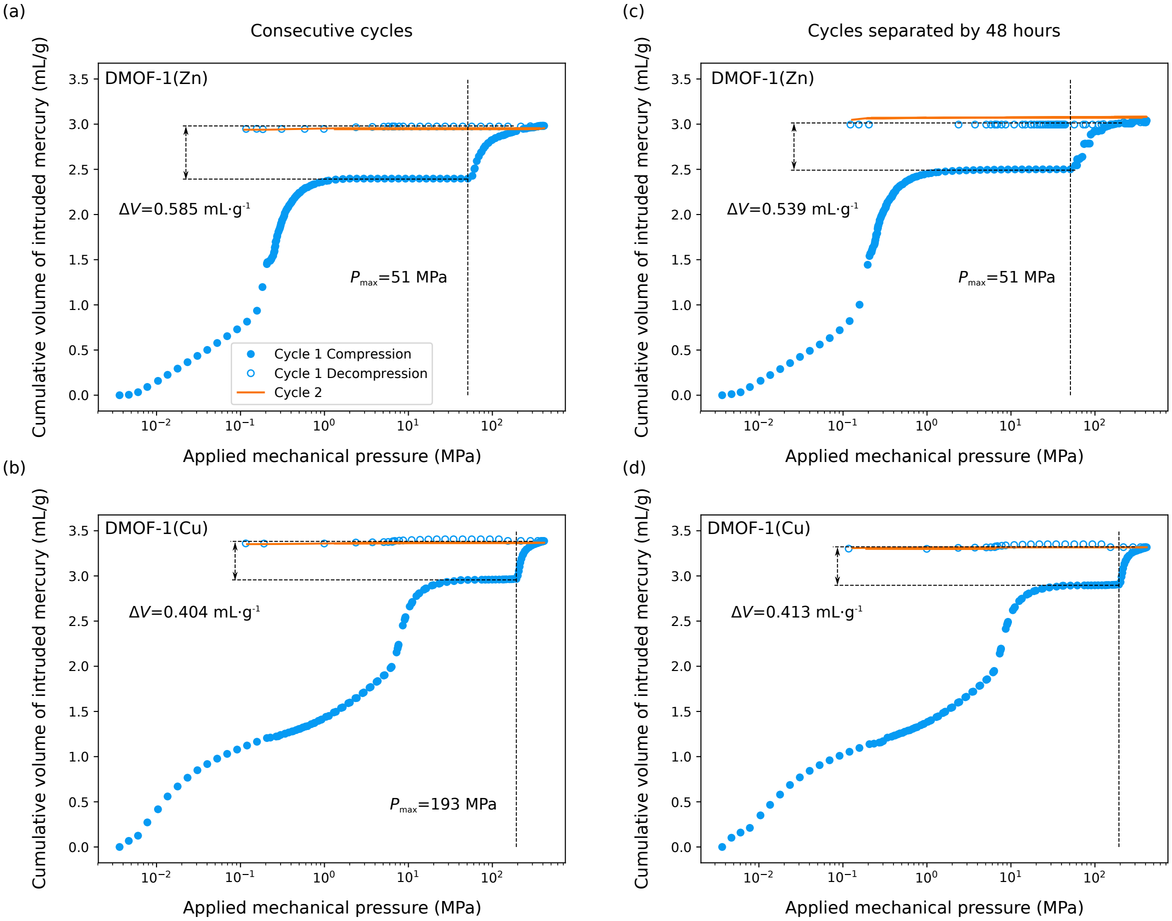

FIG. 14. Mercury intrusion curves for DMOF-1(Zn) (top row) and DMOF-1(Cu) (bottom row) for two sets of compression-decompression experiments: (i) two consecutive cycles (left) and (ii) two cycles separated by a time interval of 48 hours (right).

The bulk modulus B_0 of DMOF-1(Zn) and DMOF-1(Cu) can be estimated from the compression curves using the following equation $B_0 = V_0 \left(\frac{dP}{dV}\right)$, where V_0 is the volume of the pristine phase. The bulk modulus is then related to the slope of the linear domain of the cumulative volume of intruded mercury as a function of the applied pressure, which is defined by $\alpha = \left(\frac{dV_{Hg}}{dP}\right)$. In mercury intrusion experiments, the volume V_{Hg} is expressed in volume of intruded mercury per gram of sample. Hence, this volume corresponds to $V_{Hg} = \frac{V_0 \times N_A}{Z \times M}$. Table VI summarizes the results of the linear fitting and bulk moduli estimation following the relation defined by Henke *et al.*:[36]

$$B_0 = \frac{V_0 \times N_A}{\alpha \times Z \times M}. \tag{12}$$

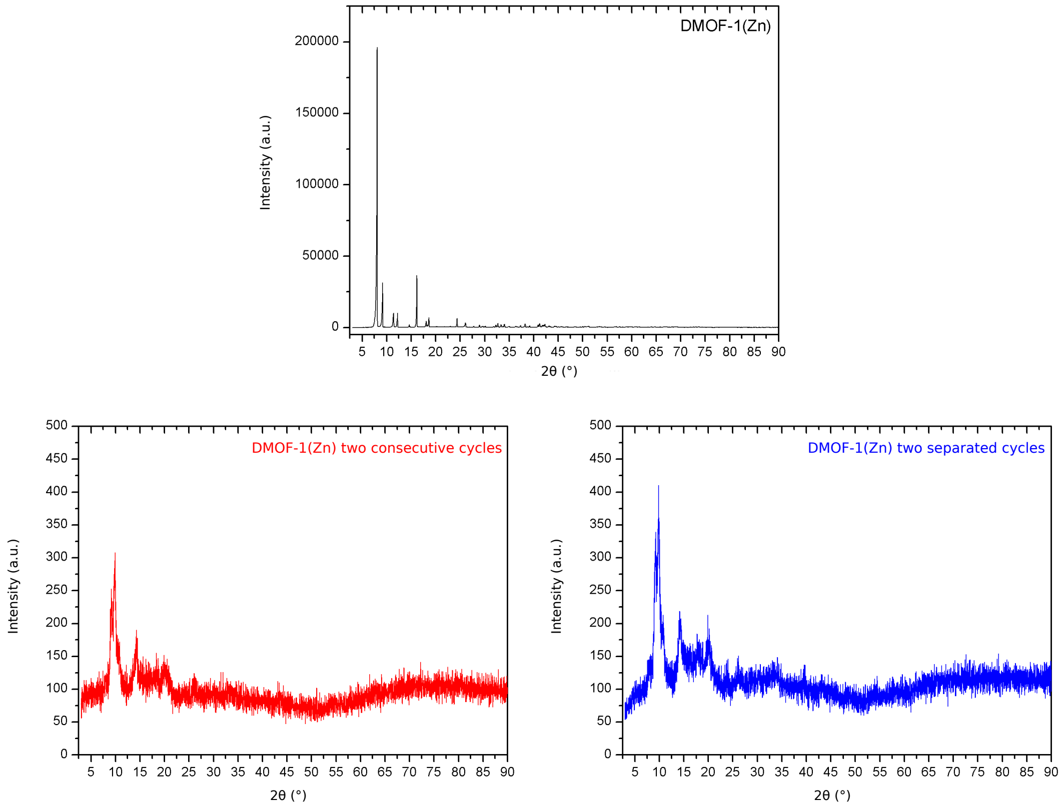

FIG. 15. A comparison of the PXRD patterns of DMOF-1(Zn) before and after Hg-compression.

PXRD measurements were also carried out after the mercury intrusion experiment on the powder collected into the penetrometer using a Jacomex P-BOX glove box ($H_2O<1$ ppm) to avoid rehydration of the powder of the solids. The data were collected 24 hours after the end of the compression. The powders were separated from the mercury and transferred into 1 mm diameter glass capillaries and sealed before PXRD collection using a PANalytical X'Pert equipped with an X'Celerator derector and a Si (111) monochromator (Cu-$K_{\alpha 1}$ wavelength, $\lambda = 1.54059$ Åwith an operating voltage of 40 kV and a beam current of 40 mA). Figures 15 and 16 show the corresponding PXRD patterns, which suggest an amorphisation of the DMOF-1 solids after compression.

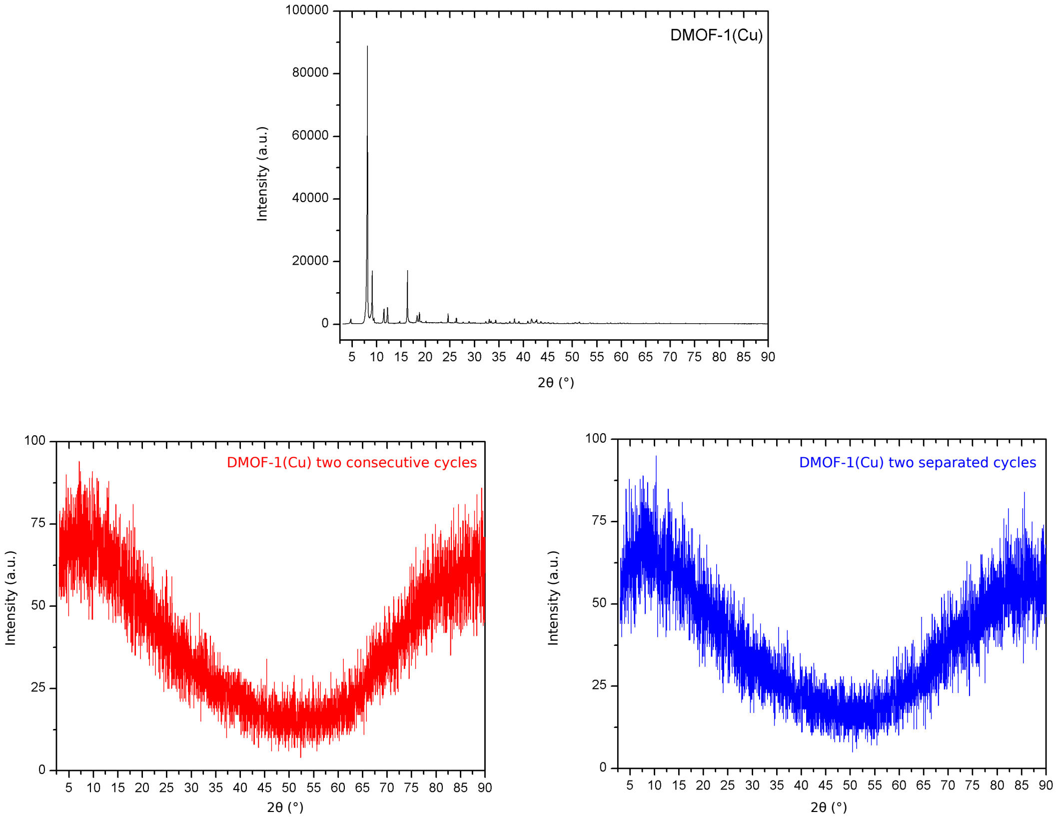

FIG. 16. A comparison of the PXRD patterns of DMOF-1(Cu) before and after Hg-compression.

IV. Structures of DMOF-1(Zn) and DMOF-1(Cu)

TABLE VII. Lattice parameters of DMOF-1(Cu) and DMOF-1(Zn).

material	method	a (Å)	b (Å)	c (Å)	α (°)	β (°)	γ (°)	V (Å^3)
DMOF-1(Cu) (this work)	PBE+D3(BJ)	15.47	9.72	15.44	90.1	90.0	90.0	2320
DMOF-1(Cu) (this work)	XRD (298 K)	15.32	9.65	15.32	90.0	90.0	90.0	2266
DMOF-1(Cu)	XRD (298 K) [37]	15.31	9.64	15.31	90.0	90.0	90.0	2259
DMOF-1(Zn) (this work)	PBE+D3(BJ)	15.61	9.57	15.59	90.0	90.0	90.0	2328
DMOF-1(Zn) (this work)	XRD (298 K)	15.46	9.62	15.46	90.0	90.0	90.0	2301
DMOF-1(Zn) [33]	SC XRD (223 K)	15.46	9.61	15.46	90.0	90.0	90.0	2295
DMOF-1(Zn) [38]	XRD (298 K)	15.47	9.61	15.47	90.0	90.0	90.0	2301
DMOF-1(Zn) [39]	XRD (298 K)	15.46	9.61	15.46	90.0	90.0	90.0	2294
DMOF-1(Zn) [40]	FF MD (223 K)	15.5±0.2	9.6±0.1	15.5±0.2				
DMOF-1(Zn)·2C_6H_6 [33]	SC XRD (223 K)	17.07	9.67	13.50	90.0	90.0	90.0	2228
DMOF-1(Zn)·3C_6H_6 [38]	XRD (298 K)	16.51	9.71	14.35	90.0	90.0	90.0	2301
DMOF-1(Zn)·3IPA [39]	XRD (298 K)	16.11	9.32	12.04	90.0	90.0	90.0	1808
DMOF-1(Zn)·4.5IPA [39]	XRD (298 K)	15.39	9.58	15.39	90.0	90.0	90.0	2270

TABLE VIII. An overview of published DMOF-1 materials and functionalized forms.

material	pore angel α ($^\circ$)	phase	V (Å^3)
DMOF-1(Cu) [37]	90	op	2259
DMOF-1(Zn) [41]	90	op	2339
DMOF-1(Zn) [39]	90	op	2294
DMOF-1(Zn) + azobenzene [41]	67	lp	2084
DMOF-1(Zn) + distyrylbenzene [42]	75	lp	2157
DMOF-1(Zn) + benzene [33]	77	lp	2228
DMOF-1(Zn) + benzene (100 K) [38]	76	lp	2203
DMOF-1(Zn) + benzene (298 K) [38]	82	lp	2301
DMOF-1(Zn) + dimethylformamide [33]	90	op	2184
DMOF-1(Zn) + dimethylformamide (298 K) [38]	90	op	2184
DMOF-1(Zn) + isopropyl alcohol [39]	74	lp	1808
DMOF-1(Zn) + isopropyl alcohol [43]	90	op	2269
DMOF-1(Co) + dimethylformamide (296 K) [44]	90	op	2217
DMOF-1(Co) + dimethylformamide (296 K, 1.3 GPa) [44]	90	op	2025
DMOF-1(Zn) **1** (2,5-BME-bdc) (as) [45]	80	lp	2284
DMOF-1(Zn) **1** (2,5-BME-bdc) (dry) [45]	60	np	1931
DMOF-1(Zn) **1** (2,5-BME-bdc) (303 K) [46]	60	np	1927
DMOF-1(Zn) **1** (2,5-BME-bdc) (493 K) [46]	90	op	2302
DMOF-1(Zn) **1** (2,5-BME-bdc) (195 K) [47]	59	np	1936
DMOF-1(Zn) **1** (2,5-BME-bdc) (195 K) [47]	80	lp	2333
DMOF-1(Zn) **3** (DE-bdc) (as) [45]	87	lp	2286
DMOF-1(Zn) **3** (DE-bdc) (dry) [45]	55	np	1776
DMOF-1(Zn) **4** (DP-bdc) (as) [45]	82	lp	2293
DMOF-1(Zn) **4** (DP-bdc) (dry) [45]	58	np	1847
DMOF-1(Zn) **5** (DiP-bdc) (as) [45]	90	op	2319
DMOF-1(Zn) **5** (DiP-bdc) (dry) [45]	57	np	1823
DMOF-1(Zn) **6** (DB-bdc) (as) [45]	90	op	2308
DMOF-1(Zn) **6** (DB-bdc) (dry) [45]	61	np	1978
DMOF-1(Zn) **2** (DB-bdc) (303 K) [46]	62	np	1977
DMOF-1(Zn) **2** (DB-bdc) (473 K) [46]	90	op	2295
DMOF-1(Zn) **5** (DB-bdc) (195 K) [47]	61	np	2000
DMOF-1(Zn) **5** (DB-bdc) (195 K) [47]	90	op	2308
DMOF-1(Zn) **8** (BA-bdc) (as) [45]	90	op	2298
DMOF-1(Zn) **8** (BA-bdc) (dry) [45]	55	np	1789
DMOF-1(Zn) **9** (BPy-bdc) (as) [45]	90	op	2302
DMOF-1(Zn) **9** (BPy-bdc) (dry) [45]	50	np	1658
DMOF-1(Cu) (2,5-BME-bdc) (as) [48]	90	op	2264
DMOF-1(Cu) (2,5-BME-bdc) (dry) [48]	63	np	2024
DMOF-1(Cu) (2,5-BME-bdc) (1 bar CO_2) [48]	81	lp	2190

[1] G. Kresse and J. Furthmüller, “Efficient iterative schemes for ab initio total-energy calculations using a plane-wave basis set,” Phys. Rev. B **54**, 11169 (1996).

[2] G. Kresse and D. Joubert, “From ultrasoft pseudopotentials to the projector augmented-wave method,” Phys. Rev. B **59**, 1758 (1999).

[3] J. P. Perdew, K. Burke, and M. Ernzerhof, “Generalized gradient approximation made simple,” Phys. Rev. Lett. **77**, 3865 (1996).

[4] S. Grimme, J. Antony, S. Ehrlich, and H. Krieg, “A consistent and accurate ab initio parametrization of density functional dispersion correction (DFT-D) for the 94 elements H-Pu,” J. Chem. Phys. **132**, 15104 (2010).

[5] S. Grimme, S. Ehrlich, and L. Goerigk, “Effect of the damping function in dispersion corrected density functional theory,” J. Comput. Chem. **132**, 1456–1465 (2011).

[6] J. Wieme, K. Lejaeghere, G. Kresse, and V. Van Speybroeck, “Tuning the balance between dispersion and entropy to design temperature-responsive flexible metal-organic frameworks,” Nat. Commun. **9**, 4899 (2018).

[7] B. M. Axilrod and E. Teller, “Interaction of the van der Waals type between three atoms,” J. Chem. Phys. **11**, 1943 (1943).

[8] Y. Muto, “Force between nonpolar molecules,” Proc. Phys. Math. Soc. Jpn. **17**, 629 (1944).

[9] “Dft-d3,”.

[10] J. Moellmann and S. Grimme, “Dft-d3 study of some molecular crystals,” J. Phys. Chem. C **118**, 7615–7621 (2014).

[11] D. E. P. Vanpoucke, K. Lejaeghere, V. Van Speybroeck, M. Waroquier, and A. Ghysels, “Mechanical properties from periodic plane wave quantum mechanical codes: the challenge of the flexible nanoporous MIL-47(V) framework,” J. Phys. Chem. C **119**, 23752–23766 (2015).

[12] P. Vinet, J. Ferrante, J. H. Rose, and J. R. Smith, “Compressibility of solids,” J. Geophys. Res. **92**, 9319–9325 (1987).

[13] D. E. P. Vanpoucke, J. W. Jaeken, S. De Baerdemacker, K. Lejaeghere, and V. Van Speybroeck, “Quasi-1D physics in metal-organic frameworks: MIL-47(V) from first principles,” Beilstein J. Nanotechnol. **5**, 1738–1748 (2014).

[14] W. Heisenberg, “Zur theorie des ferromagnetismus,” Eur. Phys. J. A **49**, 619–636 (1928).

[15] P. A. M. Dirac, "Quantum mechanics of many-electron systems," Proc. R. Soc. London, Ser. A **123**, 714–733 (1929).

[16] J. H. Van Vleck, "A survey of the theory of ferromagnetism," Rev. Mod. Phys. **17**, 27 (1945).

[17] S. G. Kozlova, D. G. Samsonenko, I. A. Tkachenko, A. B. Slobodyuk, D. A. Stepnov, and A. S. Yunoshev, "Magnetic properties in metal-organic framework compounds $[M_2(C_8H_4O_4)_2{\cdot}C_6H_{12}N_2]$ (M=Cu, Ni, Co)," Phys. Status Solidi B **253**, 2252–2256 (2016).

[18] L. Vanduyfhuys, S. Vandenbrande, T. Verstraelen, R. Schmid, M. Waroquier, and V. Van Speybroeck, "QuickFF: A program for a quick and easy derivation of force fields for metal-organic frameworks from ab initio input," J. Comput. Chem. **36**, 1015–1027 (2015).

[19] L. Vanduyfhuys, S. Vandenbrande, J. Wieme, M. Waroquier, T. Verstraelen, and V. Van Speybroeck, "Extension of the QuickFF force field protocol for an improved accuracy of structural, vibrational, mechanical and thermal properties of metal-organic frameworks," J. Comput. Chem. **39**, 999–1011 (2018).

[20] L. Vanduyfhuys, S. M. J. Rogge, J. Wieme, S. Vandenbrande, G. Maurin, M. Waroquier, and V. Van Speybroeck, "Thermodynamic insight into stimuli-responsive behavior of soft porous crystals," Nat. Commun. **9**, 204 (2018).

[21] J. Chen and T. J. Martínez, "Qtpie: Charge transfer with polarization current equalization. a fluctuating charge model with correct asymptotics," Chem. Phys. Lett. **438**, 315–320 (2007).

[22] T. Verstraelen, S. Vandenbrande, F. Heidar-Zadeh, L. Vanduyfhuys, V. Van Speybroeck, M. Waroquier, and P. W. Ayers, "Minimal basis iterative stockholder: Atoms-in-molecules for force-field development," J. Chem. Theory Comput. **12**, 3894–3912 (2016).

[23] J. H. Lii and N. L. Allinger, "Molecular mechanics. The MM3 force field for hydrocarbons. 3. the van der Waals potentials and crystal data for aliphatic and aromatic hydrocarbons," J. Am. Chem. Soc. **111**, 8576–8582 (1989).

[24] N. L. Allinger, X. Zhou, and J. Bergsma, "Molecular mechanics parameters," J. Mol. Struc.-THEOCHEM **312**, 69–83 (1994).

[25] H. Sun, "Compass: An ab initio force-field optimized for condensed-phase applications - overview with details on alkane and benzene compounds," J. Phys. Chem. B **102**, 7338–7364 (1998).

[26] J. Wieme, L. Vanduyfhuys, S. M. J. Rogge, M. Waroquier, and V. Van Speybroeck, "Exploring the flexibility of MIL-47(V)-type materials using force field molecular dynamics simulations,"

J. Phys. Chem. C **120**, 14934–14947 (2016).

[27] S. M. J. Rogge, J. Wieme, L. Vanduyfhuys, T. Verstraelen, S. Vandenbrande, G. Maurin, M. Waroquier, and V. Van Speybroeck, "Thermodynamic insight in the high-pressure behavior of UiO-66: Effect of linker defects and linker expansion," Chem. Mater. **28**, 5721–5732 (2016).

[28] A. H. Larsen, J. J. Mortensen, J. Blomqvist, I. E. Castelli, R. Christensen, M. Dułak, J. Friis, M. N. Groves, B. Hammer, C. Hargus, E. D. Hermes, P. C. Jennings, P. B. Jensen, J. Kermode, J. R. Kitchin, E. L. Kolsbjerg, J. Kubal, K. Kaasbjerg, S. Lysgaard, J. B. Maronsson, T. Maxson, T. Olsen, L. Pastewka, A. Peterson, C. Rostgaard, J. Schiøtz, O. Schütt, M. Strange, K. S. Thygesen, T. Vegge, L. Vilhelmsen, M. Walter, Z. Zeng, and K. W. Jacobsen, "The atomic simulation environment - a python library for working with atoms," **29**, 273002 (2017).

[29] V. Bon, N. Klein, I. Senkovska, A. Heerwig, J. Getzschmann, D. Wallacher, I. Zizak, M. Brzhezinskaya, U. Mueller, and S. Kaskel, "Exceptional adsorption-induced cluster and network deformation in the flexible metal-organic framework DUT-8(Ni) observed by in situ X-ray diffraction and EXAFS," Phys. Chem. Chem. Phys. **17**, 17471–17479 (2015).

[30] S. M. J. Rogge, L. Vanduyfhuys, A. Ghysels, M. Waroquier, T. Verstraelen, G. Maurin, and V. Van Speybroeck, "A comparison of barostats for the mechanical characterization of metal-organic frameworks," J. Chem. Theory Comput. **11**, 5583–5597 (2015).

[31] C. R. Groom, I. J. Bruno, M. P. Lightfoot, and S. C. Ward, "The cambridge structural database," Acta Crystallograph. B **B72**, 171–179 (2016).

[32] K. Seki and W. Mori, "Syntheses and characterization of microporous coordination polymers with open frameworks," J. Phys. Chem. B **106**, 1380–1385 (2002).

[33] D. N. Dybtsev, H. Chun, and K. Kim, "Rigid and flexible: A highly porous metal-organic framework with unusual guest-dependent dynamic behavior," Angew. Chem. Int. Ed. **43**, 5033–5036 (2004).

[34] S. Chaemchuen, K. Zhou, N. A. Kabir, Y. Chen, X. Ke, G. Van Tendeloo, and F. Verpoort, "Tuning metal sites of dabco MOF for gas purification at ambient conditions," Micropor. Mesopor. Mater. **201**, 277–285 (2015).

[35] V. Petříček, M. Dušek, and L. Palatinus, "Crystallographic computing system JANA2006: General features," Z. Kristallogr. Cryst. Mater. **229**, 345–352 (2014).

[36] S. Henke, M. T. Wharmby, G. Kieslich, I. Hante, A. Schneemann, Y. Wu, D. Daisenberger,

and A. K. Cheetham, "Pore closure in zeolitic imidazolate frameworks under mechanical pressure," Chem. Sci. **9**, 1654–1660 (2018).

[37] R. Matsuda, W. Kosaka, R. Kitaura, Y. Kubota, M. Takata, and S. Kitagawa, "Microporous structures having phenylene fin: Significance of substituent groups for rotational linkers in coordination polymers," Micropor. Mesopor. Mat. **189**, 83–90 (2014).

[38] Y. Kim, R. Haldar, H. Kim, J. Koo, and K. Kim, "The guest-dependent thermal response of the flexible MOF $Zn_2(bdc)_2(dabco)$," Dalton Trans. **45**, 4187–4192 (2016).

[39] K. Uemura, Y. Yamasaki, Y. Komagawa, K. Tanaka, and H. Kita, "Two-step adsorption/desorption on a jungle-gym-type porous coordination polymer," Angew. Chem. Int. Ed. **46**, 6662–6665 (2007).

[40] J. S. Grosch and F. Paesani, "Molecular-level characterization of the breathing behavior of the jungle-gym-type DMOF-1 metal-organic framework," J. Am. Chem. Soc. **134**, 4207–4215 (2012).

[41] N. Yanai, T. Uemura, M. Inoue, R. Matsuda, T. Fukushima, M. Tsujimoto, S. Isoda, and S. Kitagawa, "Guest-to-host-transmission of structural changes for stimuli-responsive adsorption property," J. Am. Chem. Soc. **134**, 4501–4504 (2012).

[42] N. Yanai, K. Kitayama, Y. Hijikata, H. Sato, R. Matsuda, Y. Kubota, M. Takata, M. Mizuno, T. Uemura, and S. Kitagawa, "Gas detection by structural variations of fluorescent guest molecules in a flexible porous coordination polymer," Nat. Mater. **10**, 787–793 (2011).

[43] K. Uemura, Y. Yamasaki, F. Onishi, H. Kita, and M. Ebihara, "Two-step adsorption on jungle-gym-type porous coordination polymers: Dependence on hydrogen-bonding capability of adsorbates, ligand-substituent effect, and temperature," Inorg. Chem. **49**, 10133–10143 (2010).

[44] M. Andrzejewski, N. Casati, and A. Katrusiak, "Reversible pressure preamorphization of piezochromic metal-organic framework," Dalton Trans. **46**, 14795–14803 (2017).

[45] S. Henke, A. Schneemann, A. Wütscher, and R. A. Fischer, "Directing the breathing behavior of pillared-layered metal-organic frameworks via a systematic library of functionalized linkers bearing flexible substituents," J. Am. Chem. Soc. **134**, 9464–9474 (2012).

[46] S. Henke, A. Schneemann, and R. A. Fischer, "Massive anistropic thermal expansion and thermo-responsive breathing in metal-organic frameworks modulated by linker functionalization," Adv. Funct. Mater. **23**, 5990–5996 (2013).

[47] V. Bon, J. Pallmann, E. Eisbein, H. C. Hoffmann, I. Senkovska, I. Schwedler, A. Schneemann, S. Henke, D. Wallacher, R. A. Fischer, G. Seifert, E. Brunner, and S. Kaskel, "Characteristics of flexibility in metal-organic framework solid solutions of composition [$\mathrm{Zn_2(bme\text{-}bdc)}_x$(db-bdc)$_{2-x}$dabco]$_n$: In situ powder X-ray diffraction, in situ NMR spectroscopy, and molecular dynamics simulations," Micropor. Mesopor. Mat. , 64–74 (2015).

[48] A. Schneemann, P. Vervoorts, I. Hante, M. Tu, S. Wannapaiboon, C. Sternemann, M. Paulus, D. C. F. Wieland, S. Henke, and R. A. Fischer, "Different breathing mechanisms in flexible pillared-layered metal-organic frameworks: Impact of the metal center," Chem. Mater. **30**, 1667–1676 (2018).